Organic Electronics 13 (2012) 945–953

Contents lists available at SciVerse ScienceDirect

Organic Electronics

journal homepage: www.elsevier.com/locate/orgel

An efficient inverted organic solar cell with improved ZnO and gold contact layers

Bobak Gholamkhass, Nima Mohseni Kiasari, Peyman Servati *

Department of Electrical and Computer Engineering, University of British Columbia, 2332 Main Mall, Vancouver, BC, Canada V6T 1Z4

ARTICLE INFO

Article history:
Received 21 December 2011
Accepted 11 February 2012
Available online 7 March 2012

Keywords:
Bulk heterojunction
Inverted solar cells
Organic photovoltaics
Thin films

ABSTRACT

This paper presents a high efficiency (~3.8%) inverted organic photovoltaic devices based on a P3HT:PCBM bulk heterojunction (BHJ) blend with improved electron- and hole-selective contact layers. Zinc oxide (ZnO) nanoparticle films with different thicknesses are deposited on the transparent electrodes as a nano-porous electron-selective contact layer. A thin gold film is used between the BHJ photoactive layer and the poly(3,4-ethylenedioxythiophene) poly(styrenesulfonate) (PEDOT:PSS), which improves the wettability and significantly enhances the stability of the device (>50 days of air exposure). Photovoltaic device parameters such as power conversion efficiency (PCE) and external quantum efficiency (EQE) are systematically examined for inverted devices with different thicknesses of ZnO and gold layers in comparison to the non-inverted and reference inverted devices with no contact layers. The optimized organic devices with ZnO and Au contact layers show exceptional short circuit currents (in excess of 13 mA/cm^2), in comparison to the reference devices, which is related to increased quantum efficiency of the device observed in measured EQE experiments. These results are important for development of high efficiency and stable all-printed organic solar cells and point out the role of contact layers, in particular, ZnO conductivity and morphology in the device performance.

1. Introduction

Solar energy has been regarded as a clean and renewable resource for generation of electricity. Polymer solar energy devices have increasingly become the focus of research in recent years [1–7], since they are amenable to low cost roll-to-roll manufacturing processes by using organic or inorganic–organic hybrid inks. The power conversion efficiency (PCE) of these organic photovoltaic (OPV) devices remains low; currently, the highest recorded efficiency is approximately 8% [8]. In addition to low PCE, the short life-time of OPV devices, mainly due to the degradation of organic/conducting material interfaces, undermines their long term cost effectiveness [9]. Bulk heterojunction (BHJ) OPV device structures based on blends of a donor polymer poly(3-hexylthiophene) (P3HT) and an acceptor fullerene [6,6]-phenyl C_{61}-butyric acid methyl ester (PCBM) are considered a technological benchmark against which OPVs are often measured [10–13]. In these systems, the electron-donating polymer and electron-accepting fullerene form a nanometer-sized, interpenetrating network [14,15]. Incident light is absorbed within the photoactive BHJ layer, generating bound electron–hole pairs, i.e., "excitons". Limited to their lifetime, the excitons can diffuse to the interface of the donor and acceptor polymers, where they separate into charge carriers. The diffusion length is generally in the order of tens of nanometers [16], giving rise to a device performance that depends heavily on the nano-morphology of the BHJ layer. Major improvements in terms of stability have been achieved by developing inverted OPV devices [17–20]. In a regular device structure, holes and electrons are injected into transparent indium-tin oxide (ITO) and counter electrode (e.g., Al), respectively. In contrast, in an inverted device structure electrons are injected

* Corresponding author.
E-mail address: peymans@ece.ubc.ca (P. Servati).

1566-1199/$ - see front matter © 2012 Elsevier B.V. All rights reserved.
doi:10.1016/j.orgel.2012.02.012

into the ITO while holes are collected by the top electrode [21], which can be a less air sensitive, high work-function metal such as silver or gold. At the ITO interface, metal oxides such as TiO_2 [22] and ZnO [23–27] have been applied as an electron-selective contact with PCE of over 3%. The high electron mobility of ZnO makes it an ideal electron-selective contact layer for inverted devices [28]. It has been shown that thin films of ZnO nanoparticles can be solution-processed on ITO/glass or flexible substrates at low temperature [24], an essential requirement for all-printed devices. These devices as well as those fabricated by a high temperature sol–gel process on ITO/glass is reported to exhibit a maximum PCE of 3.6% [24], the highest values reported for inverted OPVs.

In the present study, we have focused on optimizing both electron- and hole-collecting electrodes for an inverted solar cell to demonstrate high efficiency (3.8%) and improved air stability, as schematically illustrated in Fig. 1. We have modified processing parameters for low temperature fabrication of transparent ZnO thin films by spin coating of zinc acetate dehydrate, $Zn(OAc)_2{\cdot}2H_2O$ solutions. Moreover and in order to obtain an efficient inverted OPV device, we have paid particular attention to the development of the hole transport layer, i.e., poly(3,4-ethylenedioxythiophene) poly(styrenesulfonate) (PEDOT:PSS) that is coated on top of the low surface energy P3HT:PCBM photoactive layer. A thin film of gold (2–5 nm) was thermally deposited on organic layer so as to improve wettability of the photoactive layer towards the aqueous PEDOT:PSS dispersions that present large surface tensions. The photovoltaic characteristics and stability of devices are investigated as a function of ZnO and gold contact layers, which shows significant improvement in PCE and short circuit current with the use of these contact layers.

2. Experimental section

2.1. Device fabrication

As shown in Fig. 1, the inverted OPV devices had ITO/ZnO/P3HT:PCBM/Au (2–5 nm)/PEDOT:PSS/Au (100 nm) structure with an active area of 0.2 cm^2. The fabrication steps are as follows: ITO was patterned by masking with tape and etching the exposed area with conc. HCl at 60 °C. After sequential ultra-sonic cleaning in $H_2O_2/NH_3/H_2O$ (1:1:5 v/v), deionized water, acetone and 2-propanol the substrates were dried at room temperature. The zinc acetate dehydrate $Zn(OAc)_2{\cdot}2H_2O$ (Sigma–Aldrich), 50, 100 and 125 mg/mL in methanol was then spin coated on ITO at a rate of 1000 rpm for 30 s, followed by annealing at 150–350 °C for 10 min to afford a ZnO layer with thicknesses of 25, 50 and 80 nm, respectively.

Bulk heterojunction films were deposited from a 1:1 solution of PCBM (American Dye Source Inc.) and P3HT (regioregularity ~95%, Reike Metals) in 1,2-dichlorobenzene (1,2-DCB; 99%, Sigma–Aldrich), filtered through a 0.45 μm polytetrafluoroethylene (PTFE) membrane filter (Pall Co.) prior to mixing. The blend solution was spin-cast on ZnO/ITO substrates in a glove box with a sequential rate of 250 rpm (3 s), 1000 rpm (15 s) and 1500 rpm (3 s). The films were left in a covered Petri dish to control the solvent evaporation rate (drying time: 10–20 min). A thin film of gold (2–5 nm) was thermally deposited through a shadow mask onto P3HT:PCBM film using a MBraun glovebox integrated thermal evaporator system at a 0.1 Å/s deposition rate. A PEDOT:PSS (Clevios P VP AI 4083, H.C. Starck Inc.) solution mixed with an equal amount of 2-propanol was spin coated with a sequential rate of 5000 rpm (30 s). Dilution with 2-propanol is necessary in order to improve its adhesion. The PEDOT:PSS coated substrates were transferred back to the glove box and thermally annealed at 140 °C for 10 min. Finally, gold (100 nm) was thermally deposited (at a vacuum level of ~10^{-8} Torr) through a shadow mask to complete the PV device.

2.2. Device characterization

Current–voltage (I–V) measurements of devices were conducted on a computer-controlled Keithley 2400 Source Meter. A xenon lamp (150 W, Newport Co.) equipped with an AM1.5G filter was used as the light source. The optical power was 100 mW/cm^2, measured using a broadband power meter (Newport Co.) equipped with a thermopile detector head. The external quantum efficiency (EQE) was measured using monochromatic light from a monochromator (Cornerstone 130, Newport Co.) and the inci-

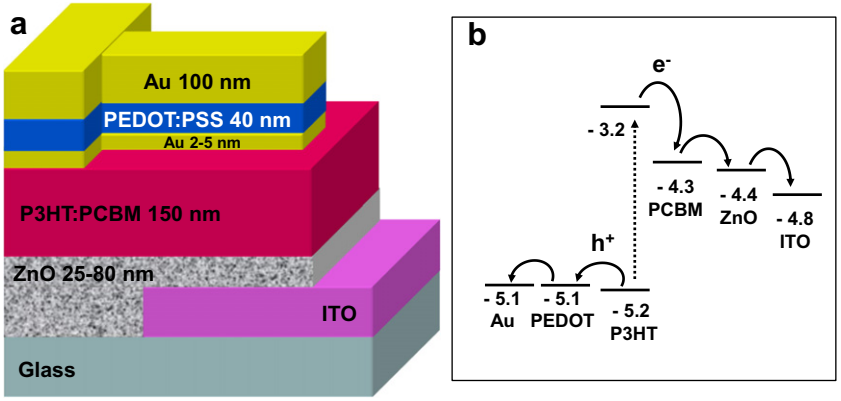

Fig. 1. Inverted solar cell device structure (a) and approximate energy level diagram (b).

dent power was measured using a power/energy meter (Newport Co.) that is also used for collecting transmittance/absorption spectra of films on ITO substrates. The EQEs were used to calculate the corresponding short-circuit current density obtained separately through efficiency testing under a 100 mA/cm^2 AM 1.5G illumination (see Supplementary data). Here, the overlap integral between EQE and AM 1.5G spectrum was calculated in the range of 330–800 nm in order to minimize the error associated with EQE arising from low incident power at shorter wavelengths. Operational stability measurements for extended testing times of up to 70 h of constant light exposure were carried out with a 100 W Sylvania tungsten lamp calibrated at 100 mW/cm^2. Bright-field transmission electron microscopic (TEM), scanning electron microscopic (SEM) and atomic force microscope (AFM) images were recorded using Hitachi 8100, Hitachi S-4700 and MFP3D-SA Asylum Research systems, respectively. An optical microscope equipped with a CCD camera was used to examine morphology of the photoactive layer. Film thicknesses were measured using an Alpha-Step IQ profilometer (KLA-Tencor). For the purpose of TEM analysis, a 40-nm layer of PEDOT:PSS was first spin coated at 5000 rpm on ITO and baked at 140 °C for 10 min in an ambient atmosphere. P3HT:PCBM layer was deposited on a ZnO/ITO substrate (with or without gold coating). The ITO substrates were immersed in a dilute HCl (5%) solution causing the ZnO layer to dissolve thus enabling the remaining polymer film to be peeled off. The floating films were picked up using 500-mesh TEM copper grids.

3. Results and discussion

3.1. Optical properties

For the preparation of ZnO contact layer, as shown in Fig. 1, a spin coated zinc acetate solution on ITO/glass substrates was converted into ZnO by a *rapid* heating at 150–350 °C on a pre-heated hot plate at ambient conditions. ZnO film, prepared at these temperatures, is practically transparent. Depending on the concentration of $Zn(OAc)_2 \cdot 2H_2O$ solution in methanol (50, 100 and 125 mg/mL), the ZnO thicknesses were varied from 25 to 50 nm and 80 nm. Fig. 2a shows the visible spectra of ZnO with transmittance of near 100% at 390–800 nm while at shorter wavelengths (350–390 nm) the transmittance is more than 75%. The wide bandgap of ZnO ensures high transmittance in this wide spectral range [29]. When a slow heating rate is applied the ZnO films became less transparent due to formation of nano-ripples as reported recently [25].

The UV–Vis absorption spectra of a blend of P3HT and PCBM (50:50 wt.%), before and after thermal annealing are shown in Fig. 2b. The absorption spectra provide evidence of extensive $\pi-\pi$ stacking of the polythiophene backbone, as indicated by absorption peaks at 525, 560, and 610 nm and an extension of the $\pi-\pi^*$ absorption band to 650 nm [30]. Upon thermal annealing at 150 °C for 1 h, the absorption spectra remain largely unchanged that is due to a slow drying process used to develop the films. The developed morphology is the kinetically stable one and thermal annealing may not necessarily contribute in enhancing the optical density [31].

3.2. Surface morphology

The SEM and AFM images of ZnO/ITO substrates with different thicknesses of ZnO layer are illustrated in Fig. 3. The ZnO nanoparticles with a relatively uniform diameter of 30–50 nm are formed and fused together after thermal treatment as described above. The surface roughness of the ZnO film appears to be a function of the thickness. It is evident that the agglomeration of ZnO nanoparticles is far more extensive in Fig. 3b for a thicker film made by spin coating of higher concentration of $Zn(OAc)_2$ solution in comparison to that in Fig. 3a. This is also supported by the AFM images presented in Fig. 3c–f, depicting the increased porosity and roughness of the ZnO layer with increasing thickness. A remarkable difference for the thicker (80-nm) ZnO film is the formation of large ZnO crystals rather than fused nanoparticles.

The photoactive BHJ blend of P3HT and PCBM (50:50 wt.%) was spin-coated on the ZnO/ITO interface using 1,2-DCB, a solvent with a high boiling point. As a result, the slow drying process enables the polymer to slowly crystalize and form an optimized morphology resulting in improved optical and electronic properties [7,31]. The morphology of P3HT:PCBM in the solid state, examined by TEM,

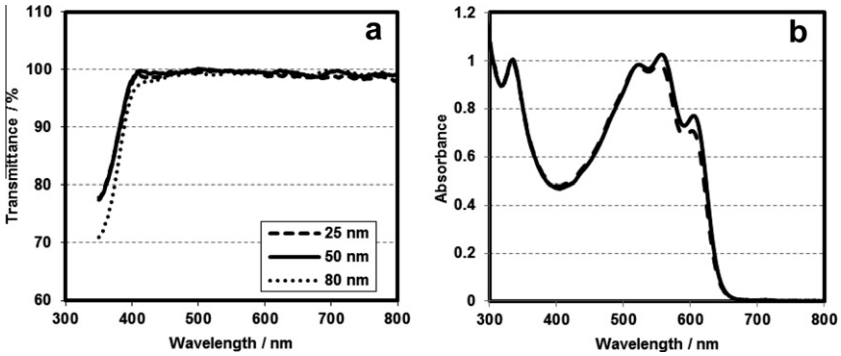

Fig. 2. Absorption spectrum of (a) ZnO on quartz substrates with thicknesses of 25 nm (dashed line), 50 nm (solid line) and 80 nm (dotted line) and (b) P3HT:PCBM on ZnO/ITO interface, spin-coated from 1,2-DCB at 1000 rpm and slow dried before (solid line) and after (dashed line) thermal annealing at 150 °C for 1 h.

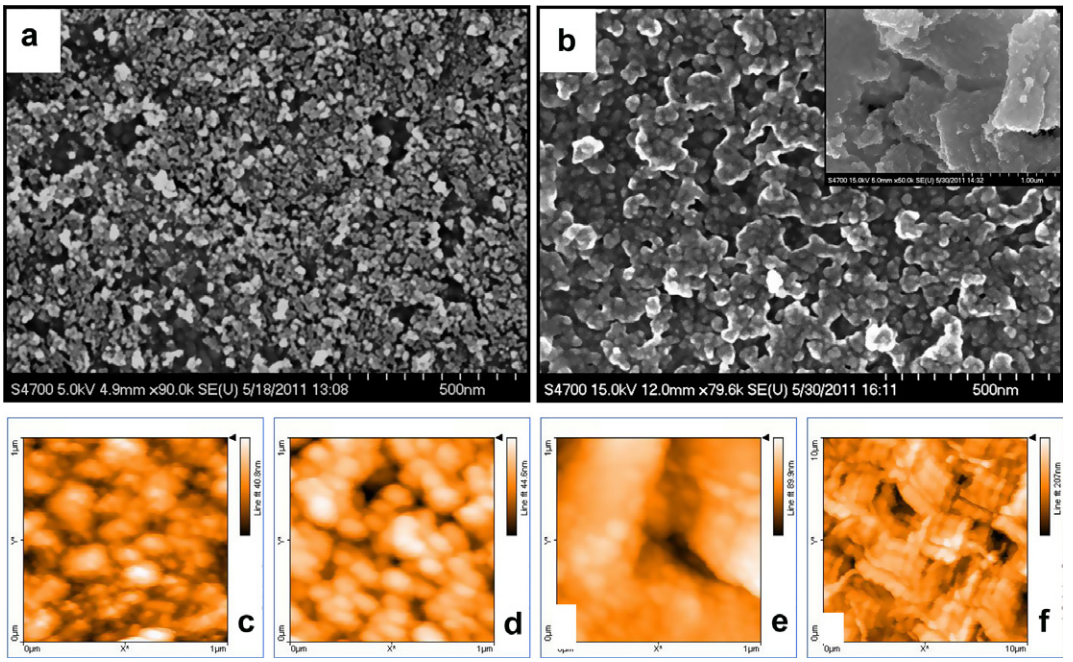

Fig. 3. SEM and AFM images of ZnO film surfaces on ITO used as hole-blocking layers in inverted OPV devices. ZnO film was prepared by spin-coating zinc acetate solution in methanol and rapid heating to 350 °C for 5 min. For SEM images, thicknesses are (a) 25 and (b) 50 nm, and for AFM images (c) 25, (d) 50 and (e) 80 nm for a 1 × 1 μm pixel. A 10 × 10 μm pixel of (e) is presented in (f). The inset in (b) shows a wider view (scale: 1 μm).

showed evidence of a binary network of P3HT and fullerene. Bright-field TEM images of the P3HT:PCBM films, before and after thermal annealing at 150 °C, are shown in Fig. 4. In the TEM image of the as-cast samples, the morphology is well developed and the donor and acceptor domains show a typical feature size of 10–20 nm. After thermal annealing at 150 °C for 1 h the domain sizes are practically the same. The TEM images reveals that thermal annealing improves the purity of the donor and acceptor network, i.e., the phase contrast becomes clearer and easily observable with a slightly larger domain size as compared to the as-cast films.

3.3. Deposition of a thin film of gold

An important technical issue in inverted OPV devices is that aqueous PEDOT:PSS does not wet the P3HT:PCBM surface effectively, even after dilution with 2-propanol (50:50 vol.%). In order to fabricate an inverted device free of pin holes and short contacts, we paid particular attention to the deposition of PEDOT:PSS layer. To improve the wettability of the photoactive layer, a thin film of gold (2–5 nm) was thermally deposited on P3HT:PCBM/ZnO/ITO interface. The TEM of the gold thin film on P3HT:PCBM is included in Fig. 4. As it is seen, the gold film is composed of nano-dots with a size ranging from 5 to 15 nm that are not connected. The height of the gold film was varied between 2 and 5 nm by controlling the deposition time at a rate of 0.1 Å/s. The advantage of the thin gold film is to improve the wettability of the photoactive layer for aqueous PEDOT:PSS that present large surface tensions [32]. Fig. 5 displays a picture of the devices after PEDOT:PSS is spin-coated on P3HT:PCBM without (devices a and b) and with 5-nm gold coating (devices c and d). Successful deposition

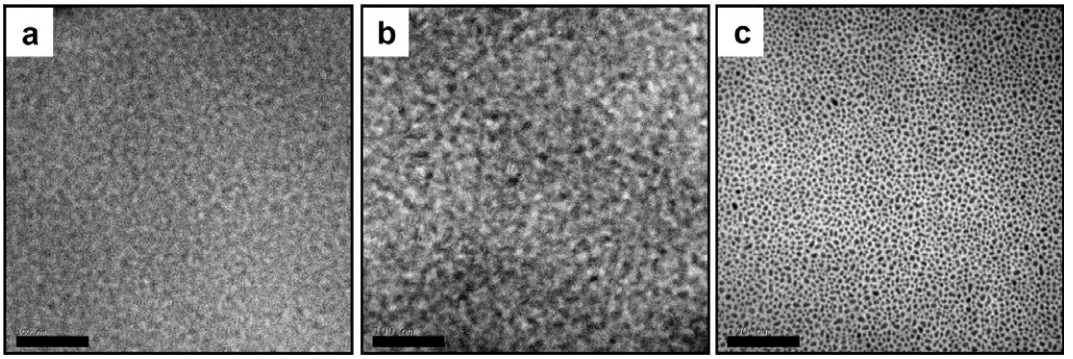

Fig. 4. TEM images of P3HT:PCBM film used as photoactive layers in inverted OPV devices (film thickness ~150 nm) on ZnO/PEDOT/ITO before (a) and after thermal annealing at 150 °C for 1 h (b), and with 2-nm gold coating (c). Scale bar is 100 nm.

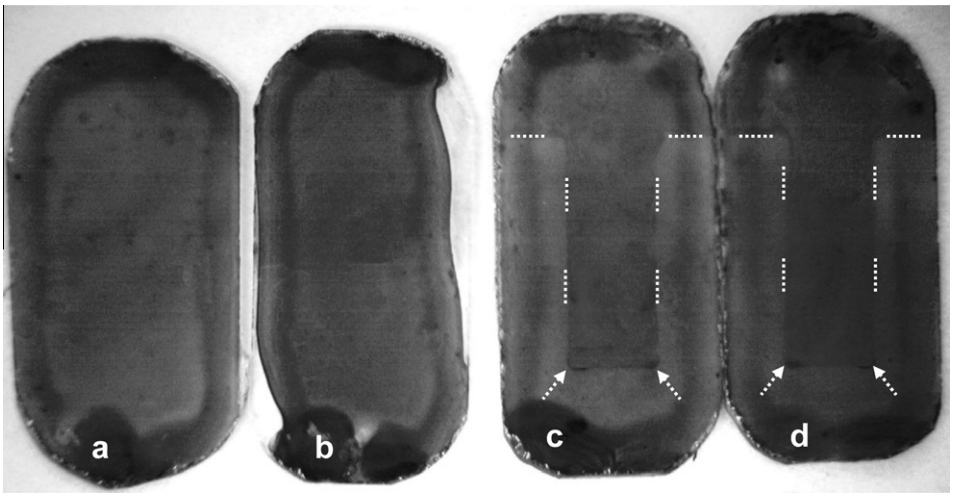

Fig. 5. A picture of the devices after PEDOT:PSS is spin-coated directly on P3HT:PCBM (a and b) and on 5-nm gold coated ones (c and d). Notice that in the gold coated devices (c and d), the deposition of PEDOT:PSS layer is visually confirmed on gold coated area (marked by arrows and dotted lines).

of PEDOT:PSS layer is visually confirmed on gold coated area. While the gold thickness has a minor impact on PV property (see below), it turned out that devices with thicker gold coating (5 nm) maintain their performance even after a long period (7 weeks in this study).

3.4. Photovoltaic performance

The PV properties of inverted devices, exposed to ambient atmosphere, were characterized by current–voltage (*I–V*) and external quantum efficiency (EQE) measurements. For comparison, a series of normal devices with a structure of glass/ITO/PEODT:PSS/P3HT:PCBM/Ca/Al was also fabricated and tested as described previously [33]. Table 1 shows the highest and average PV performances for normal and inverted OPV devices fabricated in this work. The maximum PCE of 3.8% and 3.6% were achieved for inverted devices with a gold buffer layer of 2 and 5 nm, respectively, deposited in between the photoactive layer and PEDOT:PSS. Without the gold buffer layer PCEs are in the range of 1.9–3.0%. Fabricating the same active layer in the normal (non-inverted) device architecture using Ca (20 nm) and Al (80 nm) as the top electrode yields a PCE of 2.5%.

For the inverted devices, the fill factor (FF) varies between 0.30 and 0.54 with the higher values matching the ones reported for structurally similar inverted devices [23–27]. Increasing the thickness of the ZnO (from 25 nm) results in a typically enhanced PCE (50 nm) followed by a reduction in PCE (80 nm): for 2-nm gold coated devices, PCE of 2.2 increases to 3.8 and drops to 2.1% and for 5-nm gold coated ones, PCE of 3.2 increases to 3.6 and then drops to 3.1%. Similar trends are also observed for the short-circuit current density (J_{sc}) and FF (Table 1) that point to a trade-off between complete coverage of ITO (i.e., a low density of pin-holes) and an increase in series resistance. One of the few disadvantages of ZnO is the restriction to a rather thin film due to its low conductivity [34]. Thin layer of ZnO provides a much better electron-selective interface and ohmic cathode contact [24,35].

Table 1
Extracted parameters, short-current density (J_{sc}), open-circuit voltage (V_{oc}), fill factor (FF) and power conversion efficiency (PCE) for P3HT:PCBM (50:50 wt.%) devices. Parentheses denote average performance obtained from 24 devices tested. The calculated J_{sc} is based on the overlap integral between EQE and AM1.5G spectrum in the range of 330–800 nm.

Device type	$J_{sc}^{Calculated}$ (mA/cm^2)	$J_{sc}^{Observed}$ (mA/cm^2)	V_{oc} (V)	FF	PCE (%)
Inverted: 2-nm Au					
25-nm ZnO		11.5 (11.1)	0.62 (0.60)	0.31 (0.30)	2.2 (2.0)
50-nm ZnO	13.2	13.1 (13.0)	0.55 (0.55)	0.54 (0.45)	3.8 (3.2)
80-nm ZnO		13.1 (10.3)	0.45 (0.43)	0.39 (0.37)	2.1 (1.6)
Inverted: 5-nm Au					
25-nm ZnO		11.2 (10.5)	0.59 (0.58)	0.41 (0.33)	3.2 (2.1)
50-nm ZnO	13.3	12.5 (12.0)	0.55 (0.52)	0.54 (0.50)	3.6 (3.3)
80-nm ZnO		12.3 (10.9)	0.50 (0.51)	0.50 (0.48)	3.1 (2.9)
Inverted without Au					
25-nm ZnO		11.1 (10.9)	0.52 (0.52)	0.47 (0.42)	2.7 (2.4)
50-nm ZnO	12.3	12.5 (2.1)	0.50 (0.47)	0.52 (0.45)	3.0 (2.5)
80-nm ZnO		10.9 (10.8)	0.44 (0.43)	0.40 (0.39)	1.9 (1.8)
Normal	9.8	9.8 (9.6)	0.61 (0.60)	0.45 (0.40)	2.5 (2.3)

Based on the result of this study, an optimized performance is achieved for a ZnO film thickness of 50 ± 10 nm.

In these devices, the open-circuit voltage (V_{oc}) strongly depends on the ZnO and the gold layer thicknesses; the thicker the films are the lower the V_{oc}. A similar observation is also reported for layered ZnO/poly[2-methoxy-5-(2′-ethyl-hexyloxy)-1,4-phenylenevinylene] (MEH:PPV) composite solar cells recently [36]. Therefore, as the thickness of ZnO film increases, the main loss in the overall performance can be attributed to a reduction in V_{oc}. The V_{oc} is determined by the energy difference between the highest occupied molecular orbital (HOMO) of the donor and the lowest unoccupied one (LUMO) of the acceptor components [37]. It also shows a weak dependence on the work-function difference of the two electrodes and Fermi-level pinning [38]. For a normal device architecture based on blends of P3HT and PCBM the V_{oc} can be estimated by [37]:

$$V_{OC} = (1/e)(|E_{P3HT}(\text{HOMO})| - |E_{PCBM}(\text{LUMO})|) - 0.3\ \text{V} \quad (1)$$

Here, e is the elementary charge and E_{P3HT} (−5.2 eV) and E_{PCBM} (−4.3 eV) are the HOMO and LUMO levels of each component, respectively. The value of 0.3 V, an empirical factor discussed in details by Scharber et al. [37], is the difference between the built-in potential and the V_{oc} that is originated by the dark I–V curve of the photodiode. Here, we postulate a likely scenario for a thicker ZnO film, where an additional PN heterojunction is present for charge separation and photocurrent generation. Namely, the P3HT:ZnO heterojunction rather than P3HT:PCBM is gradually becoming the dominant one in defining the V_{oc} when the porosity of the ZnO layer is increased (Fig. 3). In a similar study, low V_{oc} of hybrid P3HT/ZnO nanofiber PV devices was attributed to the presence of midgap states on the surface of the ZnO resulting in surface pinning of the Fermi level [39]. Based on the approximate energy diagram (Fig. 1), this assumption yields a V_{oc} of 0.5 V for the inverted devices (free of pin-holes and defects) using:

$$V_{OC} = (1/e)(|E_{P3HT}(\text{HOMO})| - |E_{ZnO}(\text{CB})|) - 0.3\ \text{V} \quad (2)$$

where E_{ZnO}(CB) is the conduction band energy of ZnO (∼−4.4 eV). Optical interference and light scattering effects, strongly depending on the ZnO layer thickness, can also contribute in reducing the intensity of light reaching the photoactive layer [40]—specifically, in the wavelength range of 300–400 nm where ZnO absorbs/scatters the light (Fig. 2)—reducing the V_{oc} even further.

Fig. 6 depicts the I–V characteristics for two devices with the highest PCE in this work. The observed J_{sc} and PCE for these devices are among the highest reported values for an inverted OPV device (2-nm gold film: J_{sc} = 13.1 mA/cm^2, PCE = 3.8% and 5-nm; J_{sc} = 12.5 mA/cm^2, PCE = 3.6%). The increase in J_{sc} is responsible for a remarkable improvement in PV performance of these devices compared to that of regular or the inverted ones without gold buffer layer (Table 1). It must be noted that for most of the devices the observed J_{sc}'s closely match the calculated values from the overlap integral between EQE and AM1.5G solar spectrum within ±0.2 mA/cm^2 (see Table 1 and Supplementary data).

The EQE of the inverted and normal devices are shown in Fig. 7. For all of these devices, an efficient capturing of photo-generated excitons within the range of 400–600 nm is confirmed with EQE reaching a maximum value of 0.6 between 500 and 550 nm. EQEs are calculated based on incident power reaching the active layer when ZnO/ITO and ITO substrates were used for power measurements. As it is seen in Fig. 7, the apparent EQE (filled circles) which is calculated based on a monochromatic light intensity after it passes through a ZnO/ITO substrate, and reaches the active layer, is higher. A detailed inspection of these spectra reveals that for all the inverted OPV devices, the EQE value in the 300–400 nm range is lower than that of a normal device that is in agreement with the transmittance spectra of ZnO films (Fig. 2a). Therefore, inverted OPV devices with a thicker ZnO do suffer from reduced incident power. However, the reduction in photo-generated current is estimated at ∼4% based on the overlap integral within the range of 300–400 nm. On the other hand, the EQE values of inverted devices with 2 and 5 nm of gold layer are larger

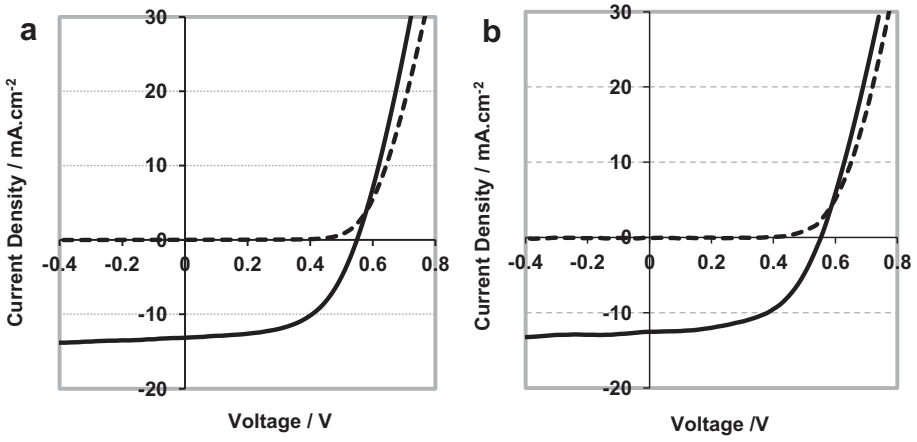

Fig. 6. Current–voltage characterization of the inverted OPV devices with the highest efficiency among each series with (a) 2 and (b) 5 nm of gold coating on P3HT:PCBM/ZnO/ITO interface. Dashed and solid lines represent dark and photocurrent, respectively. The PV parameters for each device are: (a) V_{oc} = 0.55 V, J_{sc} = 13.1 mA/cm^2, FF = 0.54 and PCE = 3.8% and (b) V_{oc} = 0.55 V, J_{sc} = 12.5 mA/cm^2, FF = 0.54 and PCE = 3.6%.

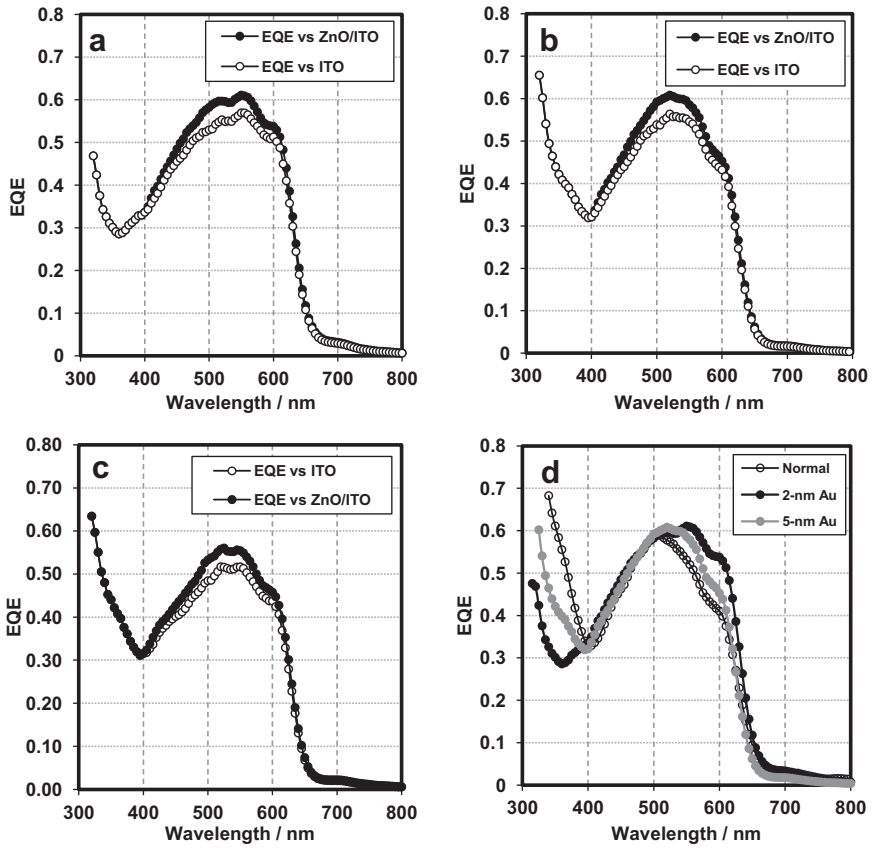

Fig. 7. External quantum efficiency (EQE) of the inverted OPV devices with a 50-nm ZnO layer for (a) 2-nm, (b) 5-nm and (c) without gold buffer layer, and (d) a normal P3HT:PCBM device that is superimposed to those of (a) and (b), showing improvement in EQE in 500–650 nm range of the spectrum consistent with the observed higher short circuit current. Filled and open circles represent the EQE value calculated based on incident power when ZnO/ITO and ITO substrates, respectively, were used for power measurements.

than that of a normal device at wavelengths longer than 400 nm (Fig. 7d) resulting in an increase of ~8% in photocurrent in the 400–800 nm range. The improved performance of inverted OPV devices (in terms of increased short circuit current and PCE) is therefore attributed to an efficient charge collection at both top and bottom contact layers. The optimization of processing parameters and formation of a transparent ZnO thin film is the key issue in developing high efficiency inverted OPV devices.

3.5. Device stability

The devices were subjected to a two-stage long-term stability test. In the first stage, devices were exposed to air for 7 weeks, during which their performance was tested periodically. After 7 weeks, in the second stage, they were illuminated with uninterrupted white light at 100 mW/cm^2 of incident power in air using a tungsten lamp filtered through AM1.5G filter. The temperature of the device holder was also monitored during light exposure (~38 ± 2 °C). Fig. 8 illustrates the PCE of the inverted OPV devices with 2- and 5-nm gold layer during the long-term test, displaying a significantly better stability for the latter in the first stage of experiment when they are exposed to ambient conditions. Namely, the PCE of the device with 5-nm gold under the PEDOT:PSS remains unchanged (at ~3.6%) after 50 days. The stability of PCEs monitored under white light exposure, however, are less promising. After 50 and 70 h of light exposure, the PCE of 2- and 5-nm gold layer devices dropped to <0.1 and 1.3%, respectively (see Supporting Information). This two stage experiment helps to separate the role of ambient and light exposure on stability of the device.

As it has been reported in the literature, thin films of P3HT:PCBM undergo gross phase separation at elevated temperatures as illustrated by the growth of large PCBM crystals—a process that reduces the interface between the donor polymer and acceptor fullerene [33,41–44]. Fig. 8 also shows microscopic images of a P3HT:PCBM film on 50-nm ZnO/ITO substrates before and after it is irradiated with white light as well as a thermally annealed film (at 150 °C for 1 h). Under white light illumination, the thermal energy transferred to the blend accelerates the phase separation process causing macro-phase segregation of the blend constituents, i.e., formation of PCBM crystals (Fig. 8d). This process is very similar but not as catastrophic as in samples annealed thermally at 150 °C for 1 h (Fig. 8e). The outcome is a slow degradation of the performance that needs to be addressed in order to improve the long-term stability of these inverted OPV devices.

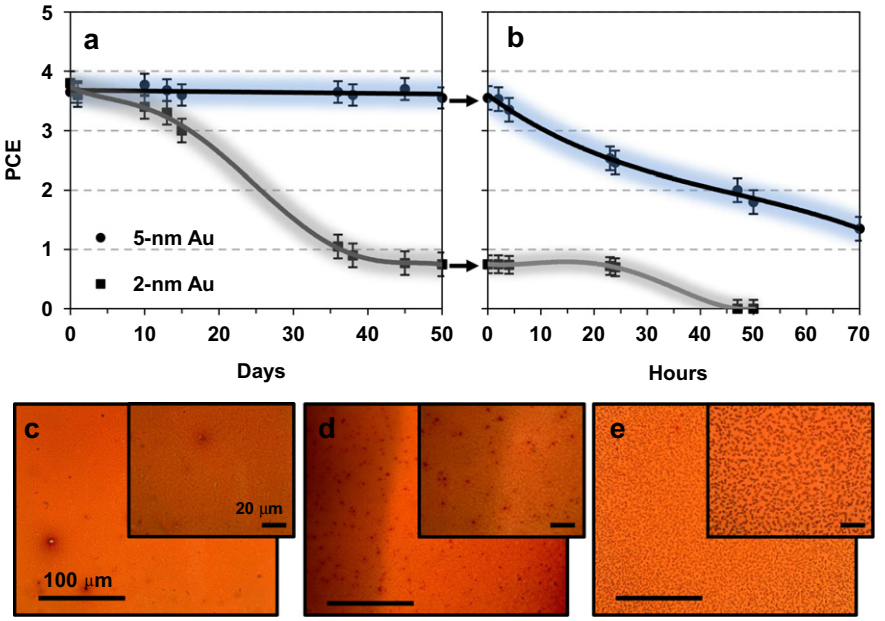

Fig. 8. Upper panel: power conversion efficiency (PCE) of non-encapsulated inverted OPV devices (a) stored in air under ambient conditions and (b) exposed to 100 mW/cm^2 of incident white light. Lines and soft-edges are drawn as a guide for trends in PCE and its error margin, respectively. Lower panel: microscopic images of a P3HT:PCBM film on 50-nm ZnO/ITO substrates for (c) as-cast, (d) exposed to air (50 days) and white light (100 mW/cm^2, 70 h), and (c) a thermally annealed film at 150 °C for 1 h. Dark area in (d) is the device active area with gold coating.

4. Conclusion

Electronic contact layers are critically important in determining how an optoelectronic device operates (in terms of electrical and optical performance), and as such, play a critical role in the photovoltaic performance of OPV devices. This paper presents inverted OPV devices with significantly improved performance in terms of efficiency (3.8%) and stability, by systematic development of contact layers. ZnO nano-porous films were investigated as electron-selective contact layer on the ITO transparent electrode. While some absorption loss in high energy photons are observed, the short-circuit current density is significantly improved (~13 mA/cm^2) for a ZnO contact layer with a thickness of 50 nm. Thicker ZnO films suppress the performance due to the low conductivity of this contact layer, increased loss of high energy photons, and reduced open circuit voltage possibly indebted to the parasitic role of ZnO:P3HT heterojunctions. A thin gold film deposited under PEDOT:PSS has shown to be highly effective in improving the wettability of BHJ layer for PEDOT:PSS deposition, resulting in improved efficiency and stability of the device. These results highlight the significant role of contact layers and device engineering in increasing the efficiency and stability of OPV devices.

Acknowledgements

The authors would like to acknowledge the financial support of Natural Sciences and Engineering Research Council (NSERC) of Canada. The authors thank Dr. Jun Shen and Rowshan Rahmanian for SEM measurements and Dr. Saeid Soltanian for lab assistances. We also acknowledge support of Prof. Steven Holdcroft at Simon Fraser University for the opportunity to utilize his lab facilities and the solar simulator system for confirming our results.

Appendix A. Supplementary data

Supplementary data associated with this article can be found, in the online version, at doi:10.1016/j.orgel.2012.02.012.

References

[1] J. Peet, A.J. Heeger, G.C. Bazan, Acc. Chem. Res. 42 (2009) 1700–1708.
[2] J.G. Xue, B.P. Rand, S. Uchida, S.R. Forrest, Adv. Mater. 17 (2005) 66–71.
[3] S. Gunes, H. Neugebauer, N.S. Sariciftci, Chem. Rev. 107 (2007) 1324–1338.
[4] F. Yang, S.R. Forrest, Acs Nano 2 (2008) 1022–1032.
[5] F.C. Krebs, Org. Electron. 10 (2009) 761–768.
[6] G. Dennler, C. Lungenschmied, H. Neugebauer, N.S. Sariciftci, A. Labouret, J. Mater. Res. 20 (2005) 3224–3233.
[7] W.L. Ma, C.Y. Yang, X. Gong, K. Lee, A.J. Heeger, Adv. Funct. Mater. 15 (2005) 1617–1622.
[8] Y.Y. Liang, Z. Xu, J.B. Xia, S.T. Tsai, Y. Wu, G. Li, C. Ray, L.P. Yu, Adv. Mater. 22 (2010) E135–E138.
[9] B. Gholamkhass, S. Holdcroft, Sol. Energy Mater. Sol. Cells 95 (2011) 3106–3113.
[10] K. Sivula, C.K. Luscombe, B.C. Thompson, J.M.J. Frechet, J. Am. Chem. Soc. 128 (2006) 13988–13989.
[11] G. Li, V. Shrotriya, J.S. Huang, Y. Yao, T. Moriarty, K. Emery, Y. Yang, Nat. Mater. 4 (2005) 864–868.
[12] K.M. Coakley, M.D. McGehee, Chem. Mater. 16 (2004) 4533–4542.
[13] H. Hoppe, N.S. Sariciftci, J. Mater. Res. 19 (2004) 1924–1945.
[14] H. Hoppe, M. Niggemann, C. Winder, J. Kraut, R. Hiesgen, A. Hinsch, D. Meissner, N.S. Sariciftci, Adv. Funct. Mater. 14 (2004) 1005–1011.
[15] S. Barrau, V. Andersson, F. Zhang, S. Masich, J. Bijleveld, M.R. Andersson, O. Inganäs, Macromolecules 42 (2009) 4646–4650.

[16] P.E. Shaw, A. Ruseckas, I.D.W. Samuel, Adv. Mater. 20 (2008) 3516–3520.
[17] M.S. White, D.C. Olson, S.E. Shaheen, N. Kopidakis, D.S. Ginley, Appl. Phys. Lett. 89 (2006) 143517.
[18] Y. Sahin, S. Alem, R. de Bettignies, J.-M. Nunzi, Thin Solid Films 476 (2005) 340–343.
[19] M.Y. Song, K.J. Kim, D.Y. Kim, Sol. Energy Mater. Sol. Cells 85 (2005) 31–39.
[20] A. Watanabe, A. Kasuya, Thin Solid Films 483 (2005) 358–366.
[21] L.M. Chen, Z.R. Hong, G. Li, Y. Yang, Adv. Mater. 21 (2009) 1434–1449.
[22] G.K. Mor, K. Shankar, M. Paulose, O.K. Varghese, C.A. Grimes, Appl. Phys. Lett. 91 (2007) 152111.
[23] C. Waldauf, M. Morana, P. Denk, P. Schilinsky, K. Coakley, S.A. Choulis, C.J. Brabec, Appl. Phys. Lett. 89 (2006) 233517.
[24] S.K. Hau, H.L. Yip, N.S. Baek, J.Y. Zou, K. O'Malley, A.K.Y. Jen, Appl. Phys. Lett. 92 (2008) 253301.
[25] D.C. Lim, W.H. Shim, K.-D. Kim, H.O. Seo, J.-H. Lim, Y. Jeong, Y.D. Kim, K.H. Lee, Sol. Energy Mater. Sol. Cells 95 (2011) 3036–3040.
[26] T.T. Larsen-Olsen, E. Bundgaard, K.O. Sylvester-Hvid, F.C. Krebs, Org. Electron. 12 (2011) 364–371.
[27] P. de Bruyn, D.J.D. Moet, P.W.M. Blom, Org. Electron. 11 (2010) 1419–1422.
[28] H.L. Yip, S.K. Hau, N.S. Baek, A.K.Y. Jen, Appl. Phys. Lett. 92 (2008) 193313.
[29] U. Ozgur, Y.I. Alivov, C. Liu, A. Teke, M.A. Reshchikov, S. Dogan, V. Avrutin, S.J. Cho, H. Morkoc, J. Appl. Phys. 98 (2005) 041301.
[30] C. Winder, N.S. Sariciftci, J. Mater. Chem. 14 (2004) 1077–1086.
[31] G. Li, Y. Yao, H. Yang, V. Shrotriya, G. Yang, Y. Yang, Adv. Funct. Mater. 17 (2007) 1636–1644.
[32] F.C. Krebs, Sol. Energy Mater. Sol. Cells 92 (2008) 715–726.
[33] S. Ebadian, B. Gholamkhass, S. Shambayati, S. Holdcroft, P. Servati, Sol. Energy Mater. Sol. Cells 94 (2010) 2258–2264.
[34] T. Stubhan, H. Oh, L. Pinna, J. Krantz, I. Litzov, C.J. Brabec, Org. Electron. 12 (2011) 1539–1543.
[35] S.H. Park, A. Roy, S. Beaupre, S. Cho, N. Coates, J.S. Moon, D. Moses, M. Leclerc, K. Lee, A.J. Heeger, Nat. Photonics 3 (2009) 297–303.
[36] N.O.V. Plank, M.E. Welland, J.L. MacManus-Driscoll, L. Schmidt-Mende, Thin Solid Films 516 (2008) 7218–7222.
[37] M.C. Scharber, D. Wuhlbacher, M. Koppe, P. Denk, C. Waldauf, A.J. Heeger, C.L. Brabec, Adv. Mater. 18 (2006) 789–794.
[38] C.J. Brabec, A. Cravino, D. Meissner, N.S. Sariciftci, T. Fromherz, M.T. Rispens, L. Sanchez, J.C. Hummelen, Adv. Funct. Mater. 11 (2001) 374–380.
[39] D.C. Olson, S.E. Shaheen, R.T. Collins, D.S. Ginley, J. Phys. Chem. C 111 (2007) 16670–16678.
[40] L.J.A. Koster, V.D. Mihailetchi, R. Ramaker, P.W.M. Blom, Appl. Phys. Lett. 86 (2005) 123509.
[41] C.H. Woo, B.C. Thompson, B.J. Kim, M.F. Toney, J.M.J. Frechet, J. Am. Chem. Soc. 130 (2008) 16324–16329.
[42] B.J. Kim, Y. Miyamoto, B.W. Ma, J.M.J. Frechet, Adv. Funct. Mater. 19 (2009) 2273–2281.
[43] S. Miyanishi, K. Tajima, K. Hashimoto, Macromolecules 42 (2009) 1610–1618.
[44] B. Gholamkhass, S. Holdcroft, Chem. Mater. 22 (2010) 5371–5376.